

Impact of neutron star spin on Poynting-Robertson drag during a Type I X-ray burst

J. Speicher^{1*} †, P. C. Fragile² and D. R. Ballantyne¹

¹Center for Relativistic Astrophysics, School of Physics, Georgia Institute of Technology, 837 State Street, Atlanta, GA 30332-0430, USA

²Department of Physics & Astronomy, College of Charleston, 66 George St., Charleston, SC 29424, USA

Accepted XXX. Received YYY; in original form ZZZ

ABSTRACT

External irradiation of a neutron star (NS) accretion disc induces Poynting-Robertson (PR) drag, removing angular momentum and increasing the mass accretion rate. Recent simulations show PR drag significantly enhancing the mass accretion rate during Type I X-ray bursts, which could explain X-ray spectral features such as an increase in the persistent emission and a soft excess. However, prograde spin of the NS is expected to weaken PR drag, challenging its importance during bursts. Here, we study the effect of spin on PR drag during X-ray bursts. We run four simulations, with two assuming a non-spinning NS and two using a spin parameter of $a_* = 0.2$, corresponding to a rotation frequency of 500 Hz. For each scenario, we simulate the disc evolution subject to an X-ray burst and compare it to the evolution found with no burst. PR drag drains the inner disc region during a burst, moving the inner disc radius outward by ≈ 1.6 km in the $a_* = 0$ and by ≈ 2.2 km in the $a_* = 0.2$ simulation. The burst enhances the mass accretion rate across the innermost stable circular orbit ≈ 7.9 times when the NS is not spinning and ≈ 11.2 times when it is spinning. The explanation for this seemingly contradictory result is that the disc is closer to the NS when $a_* = 0.2$, and the resulting stronger irradiating flux offsets the weakening effect of spin on the PR drag. Hence, PR drag remains a viable explanation for the increased persistent emission and soft excess observed during X-ray bursts in spinning NS systems.

Key words: accretion, accretion discs – radiation: dynamics – stars: neutron – X-rays: binaries – X-rays: bursts

1 INTRODUCTION

Compact objects such as black holes, neutron stars, and white dwarves may accrete matter from their surroundings. If the infalling material possesses angular momentum, an accretion disc forms to transport the angular momentum outwards through viscous processes (for a review, see Abramowicz & Fragile 2013). The disc structure is often described by the α model (Shakura & Sunyaev 1973). The Newtonian model by Shakura & Sunyaev (1973) and its general relativistic counterpart by Novikov & Thorne (1973) assume no external irradiation. Despite external irradiation coming from the corona, a region of hot electrons (e.g., Galeev et al. 1979; Zdziarski & Gierliński 2004), and the neutron star surface or a boundary layer (e.g., Inogamov & Sunyaev 1999; Popham & Sunyaev 2001; Inogamov & Sunyaev 2010), these disc models offer a satisfactory description of realistic accretion discs and are often the basis of accretion disc simulations (e.g., Kubota & Makishima 2004; Kubota et al. 2005; Shafee et al. 2008; Fragile et al. 2020). However, when accretion discs are strongly irradiated by Type I X-ray bursts, the disc structure starts to diverge from the standard model.

Type I X-ray bursts can arise from neutron stars in low-mass X-ray binaries (for a review, see Lewin et al. 1993; Galloway & Keek 2021). In these binaries, neutron stars accrete matter via Roche-Lobe overflow. The accreted material, mainly hydrogen and helium, accumulates on the neutron star’s surface. The matter is gradually

compressed, increasing the accreted layer’s temperature until nuclear burning sets in. However, due to the thin-shell instability, the layer does not cool by expansion but heats up further (e.g., Schwarzschild & Härm 1965; Fujimoto et al. 1981; Yoon et al. 2004). Subsequent accretion eventually renders the nuclear burning unstable, and the accreted matter conflagrates within seconds, leading to an X-ray burst (e.g., Fujimoto et al. 1981; Narayan & Heyl 2003; Galloway & Keek 2021). During its fast exponential rise, followed by a slow exponential decay, the burst emits $\sim 10^{39} - 10^{42}$ erg of radiation into the neutron star environment (e.g., Strohmayer & Brown 2002; Kuulkers et al. 2003; Galloway et al. 2008; Degenaar et al. 2013).

The burst radiation observably impacts the accretion environment (for a review, see Degenaar et al. 2018). Observations and calculations find reduced high energy emission during bursts, which has been linked to Compton cooling of electrons in the corona (e.g., Maccarone & Coppi 2003; Ji et al. 2014; Sánchez-Fernández et al. 2020; Speicher et al. 2020). The accretion disc’s reflection spectrum also evolves over the burst’s duration. Several burst observations feature emission lines (e.g., Degenaar et al. 2013; Keek et al. 2014a, 2017; Bult et al. 2019), whose strength should evolve with the burst flux (e.g., Speicher et al. 2022). Observed evolutions in reflection spectra have been limited to superbursts, which have been used to deduce a change in disc ionization and inner accretion disc radius (e.g., Ballantyne & Strohmayer 2004; Keek et al. 2014b).

In addition, the overall amount of persistent emission changes during bursts. Worpel et al. (2013) and Worpel et al. (2015) multiplied the persistent emission by a normalization factor, f_a , and not

* E-mail: jspeicher3@gatech.edu

† NDSEG Fellow

only found that including f_a improves the fit, but also that f_a often exceeded 1. Due to its ability to improve fits, f_a has become a common burst analysis tool (e.g., Jaisawal et al. 2019; Bult et al. 2022; Güver et al. 2022a,b). Furthermore, the normalization factor has been used to accommodate a soft excess occurring at energies below 3 keV (e.g., Keek et al. 2018; Bult et al. 2019; Güver et al. 2022a,b). The enhanced normalization factors have been linked to an increased mass accretion rate, \dot{M} , caused by burst photons exerting Poynting-Robertson (PR) drag on the accretion disc. PR drag is a special relativistic effect, through which irradiation from a central source removes angular momentum from an orbiting particle (Robertson 1937). As the calculations by Walker & Meszaros (1989) and Walker (1992) showed, the additional irradiation by the burst photons causes particles to fall faster toward the neutron star, thus increasing \dot{M} .

The effect of PR drag during an X-ray burst was studied in simulations by Fragile et al. (2020). In their simulations, an X-ray burst with a peak luminosity of $L_0 = 10^{38}$ erg s⁻¹ interacted with a thin accretion disc. The increase in PR drag increased \dot{M} by over an order of magnitude. The increased mass accretion rate drained the inner accretion disc region and the inner disc radius moved outward by a few kilometers.

However, the impact of PR drag measured by Fragile et al. (2020) was under the assumption of a nonspinning neutron star, which may have made the PR drag more pronounced than in real neutron star systems. Realistically, neutron stars spin with frequencies up to ~ 700 Hz (e.g., Chakrabarty et al. 2003; Hessels et al. 2006; Bassa et al. 2017; Patruno et al. 2017). This usually prograde neutron star spin will reduce the angular velocity difference between the neutron star photon field and the gas of the disc. Hence, a prograde neutron star spin is expected to reduce the strength of PR drag and thus the mass accretion rate enhancement (e.g., Walker 1992). Since the mass accretion rate enhancement has served as an explanation for an increased persistent emission or soft excess during burst observations, it is worth reassessing whether PR drag is strong enough in spinning neutron star systems to enhance \dot{M} significantly, or whether an increase in the f_a factor is driven by other processes, such as reflection (e.g., Speicher et al. 2022).

Hence, this paper studies the importance of PR drag during an X-ray burst for a spinning neutron star, for which we extend the simulations by Fragile et al. (2020). Unless otherwise specified, all equations in this paper are written in units where $G = c = 1$. The paper is structured as follows: Sec. 2 outlines the methods relevant to our simulations. The simulation results will be presented in Sec. 3 with additional analytical calculations of PR drag provided in Sec. 4. Finally, we discuss the implications of our results in Sec. 5 with conclusions stated in Sec. 6.

2 METHODS

Our simulations extend the work by Fragile et al. (2020), which implemented an X-ray burst interacting with a thin accretion disc around a non-spinning neutron star. The neutron star spin we introduce corresponds to a rotational frequency, f_* , in the prograde direction. To highlight the effect of the neutron star spin, we select a high, yet realistic, rotational frequency of 500 Hz. The dimensionless spin parameter, a_* , is defined as

$$a_* = \frac{J}{M^2}, \quad (1)$$

where J is the angular momentum and M is the neutron star mass. We assume that J is the product of the moment of inertia and the angular

frequency ($2\pi f_*$). The relationship between the rotational frequency and the spin parameter depends on the neutron star's equation of state (EOS; e.g., Sibgatullin & Sunyaev 1998; Koliogiannis & Moustakidis 2020). We select EOS A by Cook et al. (1994), because its compactness best matches our assumed neutron star parameters. For our simulations, we choose a neutron star radius of $R_* = 10.7$ km and mass $M = 1.45 M_\odot$. Using the tabulated neutron star properties of EOS A, which relates angular frequencies, moments of inertia, and neutron star masses (see table 9 by Cook et al. 1994), we follow Sibgatullin & Sunyaev (1998) and calculate an array of spin parameters and corresponding angular velocity parameters W ,

$$W = 2\pi f_* M. \quad (2)$$

From this spin versus angular velocity parameter relationship, we can infer that the spin parameter corresponding to $f_* = 500$ Hz and $M = 1.45 M_\odot$ is $a_* \approx 0.2$.

The neutron star rotation impacts the four-momentum and stress-energy tensor of the burst photons. The photon's four-momentum is, in Boyer-Lindquist coordinates $\{t, r, \theta, \phi\}$ (e.g., Bakala et al. 2019),

$$\begin{aligned} k^t &= \Sigma^{-1} \left[ab - a^2 \sin^2 \theta + (r^2 + a^2) P \Delta^{-1} \right] \\ k^r &= \Sigma^{-1} \sqrt{R_{b,q}(r)} \\ k^\theta &= \pm \Sigma^{-1} \sqrt{\Theta_{b,q}(\theta)} \\ k^\phi &= \Sigma^{-1} (b \csc^2 \theta - a + a P \Delta^{-1}), \end{aligned} \quad (3)$$

where $P \equiv r^2 + a^2 - ba$, $\Delta \equiv r^2 - 2Mr + a^2$, and $\Sigma \equiv r^2 + a^2 \cos^2 \theta$. The terms $\Theta_{b,q}(\theta)$ and $R_{b,q}(r)$ are $\Theta_{b,q}(\theta) \equiv q + a^2 \cos^2 \theta - b^2 \cot^2 \theta$ and $R_{b,q}(r) = (r^2 + a^2 - ab)^2 - \Delta[q + (b-a)^2]$, respectively. Here, a is the specific angular momentum of the neutron star (J/M). The \pm sign in the k^θ expression (eq. 3) depends on the photon trajectory. The latitudinal photon impact parameter, q , is given as

$$\begin{aligned} q &\equiv \left(\frac{k_\theta}{k_t} \right)^2 + \left[b \tan \left(\frac{\pi}{2} - \theta \right) \right]^2 - a^2 \cos^2 \theta \\ &= b^2 \cot^2 \theta_e - a^2 \cos^2 \theta_e, \end{aligned} \quad (4)$$

while the azimuthal impact parameter, b , is

$$b \equiv -\frac{k_\phi}{k_t} = \frac{\sin^2 \theta_e [(R_*^4 + a^2 \mathcal{B}) 2\pi f_* - 2aMR_*]}{R_*^2 - 2MR_* + a(a \cos^2 \theta_e + 2MR_* 2\pi f_* \sin^2 \theta_e)}, \quad (5)$$

where θ_e is the polar emission angle. The term \mathcal{B} is given as

$$\mathcal{B} = (a^2 + R_*^2) \cos^2 \theta_e + 2MR_* \sin^2 \theta_e + R_*^2. \quad (6)$$

To match the space-time metric of the simulation, the photon momentum components are transformed from Boyer-Lindquist to Kerr-Schild coordinates. The photon 4-momentum (eq. 3) transforms as

$$\begin{aligned} k^{\tilde{t}} &= k^t + \frac{2Mr}{\Delta} k^r \\ k^{\tilde{r}} &= k^r \\ k^{\tilde{\theta}} &= k^\theta \\ k^{\tilde{\phi}} &= k^\phi + \frac{a}{\Delta} k^r. \end{aligned} \quad (7)$$

Since the simulation mesh is more refined at smaller radii and towards the equatorial plane (Fragile et al. 2020), the components $k^{\tilde{r}}$

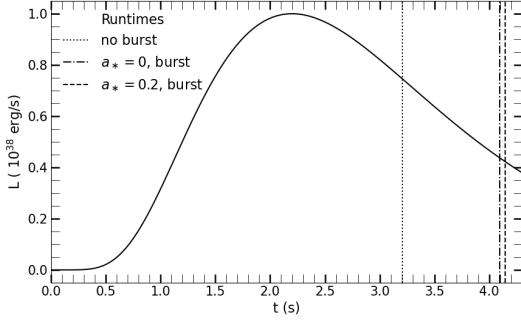


Figure 1. Burst profile (eq. 12). The vertical lines mark the runtimes of the burst (dot-dashed line for $a_* = 0$ and dashed line for $a_* = 0.2$) and no-burst (dotted line) simulations.

and $k^{\tilde{\theta}}$ are additionally converted as

$$\begin{aligned} k^{\tilde{x}_1} &= \left(\frac{\partial \tilde{r}}{\partial \tilde{x}_1} \right)^{-1} k^{\tilde{r}} \\ k^{\tilde{x}_2} &= \left(\frac{\partial \tilde{\theta}}{\partial \tilde{x}_2} \right)^{-1} k^{\tilde{\theta}}, \end{aligned} \quad (8)$$

where

$$\begin{aligned} \tilde{r} &= R_* \exp(\tilde{x}_1 - 1) \\ \tilde{\theta} &= \tilde{x}_2 + 0.25 \sin \tilde{x}_2. \end{aligned} \quad (9)$$

The coordinate \tilde{x}_2 describes the uniform latitude coordinate in the code.

The photon momentum enters the photon stress-energy tensor, $R^{\mu\nu}$, as (e.g., Bakala et al. 2019)

$$R^{\tilde{\mu}\tilde{\nu}} = \Phi^2 k^{\tilde{\mu}} k^{\tilde{\nu}}, \quad (10)$$

where the intensity parameter, Φ , is normalized so as to produce the desired integrated burst luminosity

$$L = - \int_S \sqrt{-g} R^{\tilde{r}}_{\tilde{t}} dA_{\tilde{r}}, \quad (11)$$

where $dA_{\tilde{r}}$ is the surface area element normal to the radial direction and g is the metric determinant. The luminosity is chosen to vary with time as (Fig. 1, e.g., Norris et al. 2005; Barrière et al. 2015)

$$L(t) = L_0 e^{2(\tau_1/\tau_2)^{1/2}} e^{-\frac{\tau_1}{t-t_s} - \frac{t-t_s}{\tau_2}}, \quad (12)$$

where $L_0 = 10^{38} \text{ erg s}^{-1}$, $t_s = -0.25 \text{ s}$, $\tau_1 = 6 \text{ s}$, and $\tau_2 = 1 \text{ s}$. Unlike the simulations by Fragile et al. (2020), we only consider the burst luminosity and ignore any luminosity due to accreted material hitting the neutron star surface.

Similar to the approach by Sądowski et al. (2013), we use the components $R^{\tilde{\mu}}_{\tilde{\nu}} = g_{\tilde{\mu}\tilde{\nu}} \Phi^2 k^{\tilde{r}} k^{\tilde{\nu}}$, with $g_{\tilde{\mu}\tilde{\nu}}$ being the metric, to solve the equation

$$R^{\tilde{r}}_{\tilde{\mu}} = \frac{4}{3} E_R u^{\tilde{r}}_{\tilde{R}}(u_R)_{\tilde{\mu}} + \frac{1}{3} E_R \delta^{\tilde{r}}_{\tilde{\mu}} \quad (13)$$

for the radiation energy density, E_R , in its rest frame and the radiation velocity, u_R , in an observer frame. These energy and velocity are used to inject radiation at the inner simulation boundary.

We implemented our simulations in the general relativistic hydrodynamics code *Cosmos++* (Anninos et al. 2005; Fragile et al. 2012, 2014). For each simulation, the code first initializes the gas-pressure dominant region of an α -disc with a viscosity parameter of

$\alpha = 0.025$ (e.g., Abramowicz & Fragile 2013). The discs start out in hydrostatic and thermal equilibrium. The remaining simulation space is filled with a low energy, low mass density gas with energy $3/2 \times 10^{-4} E_{\text{max}} r^{-2.5}$ and density $10^{-6} \rho_{\text{max}} r^{-1.5}$. The terms E_{max} and ρ_{max} are the maximum energy and mass density of the disc, respectively. For $a_* = 0$, $E_{\text{max}} \approx 8.2 \times 10^{14} \text{ erg cm}^{-3}$ and $\rho_{\text{max}} \approx 0.35 \text{ g cm}^{-3}$, while for $a_* = 0.2$, $E_{\text{max}} \approx 1.1 \times 10^{15} \text{ erg cm}^{-3}$ and $\rho_{\text{max}} \approx 0.43 \text{ g cm}^{-3}$. During the simulation, *Cosmos++* numerically advances the general relativistic, radiative, viscous hydrodynamics equations as outlined by Fragile et al. (2018). The simulations are two-dimensional and cover a radial range of $10.7 \text{ km} \lesssim r \lesssim 352 \text{ km}$ and $0 \lesssim \theta \lesssim \pi$, with the innermost zones lying just above the stellar surface (i.e., the neutron star surface is not in the simulation domain and always within the innermost stable circular orbit of the disc). The simulation domain is covered by a mesh subdivided into the equivalent of 384 cells in the radial direction, and 384 cells in the angular direction. The exponential cell spacing in the radial direction and a greater concentration of cells in the equatorial plane using \tilde{x}_1 and \tilde{x}_2 (eq. 9) allows a greater mesh refinement closer to the neutron star and the midplane of the disc. All simulations omit the effects of the stellar magnetic field. That is, we assume the field is weak enough to not impact the dynamics of the accretion flow.

As a change to the underlying physics described in Fragile et al. (2020), we use Planck and Rosseland mean opacity coefficients of $3.2 \times 10^{24} \text{ cm}^2 \text{ g}^{-1}$ and $8.6 \times 10^{22} \text{ cm}^2 \text{ g}^{-1}$, respectively (Hirose et al. 2009). To study the impact of spin, we ran two sets of simulations, one with spin and one without. Each set consists of a burst and a no-burst simulation. The no-burst simulations (Fig. 1, vertical dotted line) ran for $\approx 3.2 \text{ s}$, while the burst simulations (vertical dot-dashed line for $a_* = 0$ and vertical dashed line for $a_* = 0.2$) ran for $\approx 4.1 \text{ s}$.

3 RESULTS

Fig. 2 shows spacetime diagrams of the logarithm of the density-weighted gas temperature for all four simulations. In the absence of a burst, the simulated accretion discs are constant in time (upper row). Differences between these undisturbed discs arise through the impact of the neutron star spin on the spacetime. The accretion discs in the no-burst simulations terminate at the innermost stable circular orbit r_{isco} , which is spin dependent. For $a_* = 0$ (upper row, left panel), $r_{\text{isco}} \approx 12.85 \text{ km}$, and for $a_* = 0.2$ (upper row, right panel), $r_{\text{isco}} \approx 11.41 \text{ km}$. Besides the differences in r_{isco} , in the no-burst simulations the $a_* = 0.2$ disc (upper row, right panel) is hotter than the $a_* = 0$ one (upper row, left panel) at radii larger than the r_{isco} of $a_* = 0$. In the burst simulations (Fig. 2, lower row), the burst radiation heats the disc. Due to its higher steady-state temperatures (upper row, right panel), the simulated $a_* = 0.2$ disc reaches higher temperatures at radii $\gtrsim 14 \text{ km}$ compared to the $a_* = 0$ disc (lower row, left panel) during the burst. The temperature increase inflates both discs since they are pressure supported.

Another structural change due to the burst is the movement of the inner disc radius, r_{in} , to larger radii (Fig. 3, see also the expansion of the hot optically thin region colored in red in the lower row of Fig. 2). We define the location of r_{in} as the radial position where the surface density is closest to $2.5 \times 10^2 \text{ g cm}^{-2}$. This surface density value ensures that $r_{\text{in}} \approx r_{\text{isco}}$ in the no-burst simulations (magenta dotted line for $a_* = 0$, orange dot-dashed line for $a_* = 0.2$). At early times, the burst impact is negligible, and $r_{\text{in}} \approx r_{\text{isco}}$ in all simulations. As the burst luminosity increases (eq. 12, Fig. 1), the inner disc radii move outward by $\approx 1.6 \text{ km}$ in the $a_* = 0$ and by $\approx 2.2 \text{ km}$ in the $a_* = 0.2$ burst simulation.

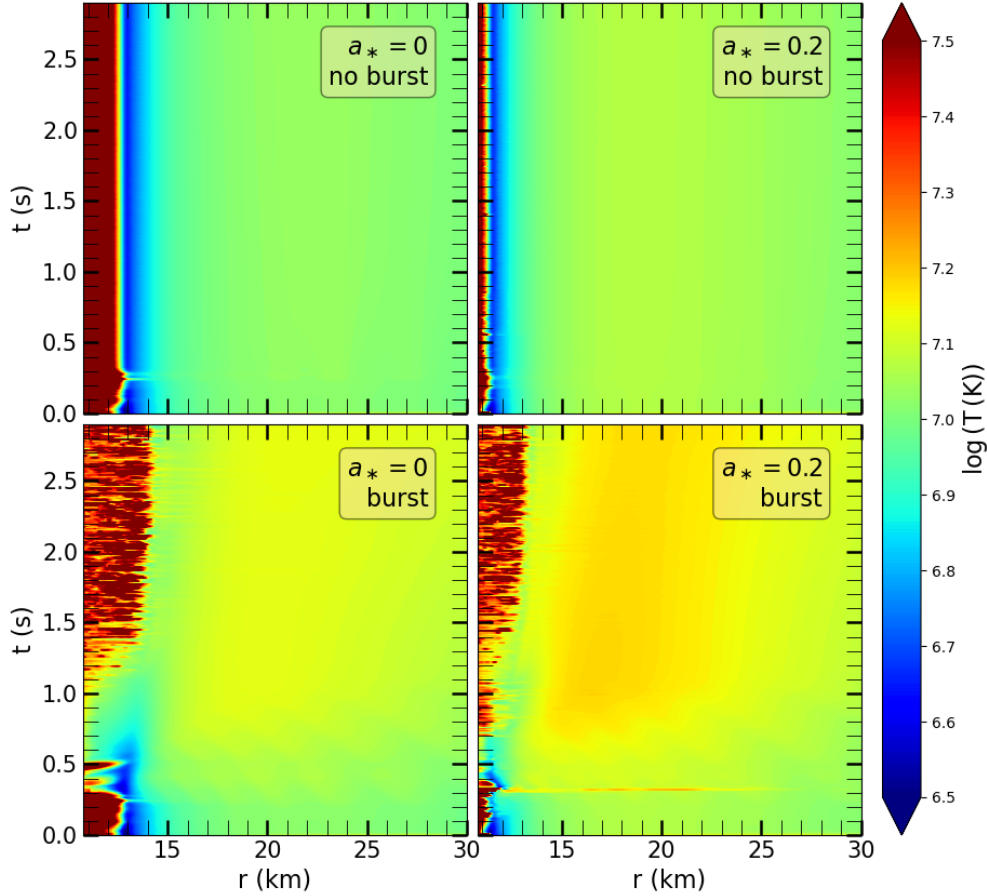


Figure 2. Spacetime diagrams of the density-weighted temperature. Top row: The temperatures remain constant in the no-burst simulations. The spin changes the spacetime and thus the accretion disc structure, moving r_{isco} closer to the neutron star in the $a_* = 0.2$ simulation (top row, right panel) than in the $a_* = 0$ one (top row, left panel). Bottom row: Due to the burst radiation, the inner disc radii recede outwards for both the $a_* = 0$ (bottom row, left panel) and the $a_* = 0.2$ (bottom row, right panel) simulations. Additionally, the burst radiation heats the discs. The final disc temperatures differ between the spin and the no-spin simulation due to the different steady-state disc structures (top row).

The movement of r_{in} is due to increased PR drag, which removes angular momentum from the disc. Fig. 4 shows the spacetime diagrams of the logarithm of the angular frequency, Ω , for the burst simulations. At $t \lesssim 1$ s, the low burst luminosity does not significantly affect the angular frequencies. Since the disc gas orbits faster closer to the neutron star, the angular frequencies increase with decreasing radii. The increasing burst strength decreases Ω at $t \gtrsim 1$ s. We find that the decrease in Ω is not smooth, but fluctuates. The decrease in Ω can be measured across larger distances with increasing burst luminosity and thus increasing r_{in} (see the blue and green stripes extending towards larger radii in Fig. 4).

Even though the evolution of Ω appears to differ between the $a_* = 0$ (Fig. 4, left panel) and $a_* = 0.2$ (Fig. 4, right panel) burst simulations, the decrease in angular frequency is comparable at their respective r_{isco} (dashed black lines in Fig. 4). For Fig. 5, we smoothed out time-dependent fluctuations by calculating the moving averages of Ω at the respective r_{isco} with an average window of $\Delta t \approx 0.71$ s before taking the ratios between the burst and the no-burst simulation

results. Following the Ω evolution shown in Fig. 4, the ratios of the smoothed frequencies decrease with increasing burst luminosity (eq. 12) and reach their minima at approximately the time of the burst peak (Fig. 1). The Ω ratio reaches a minimum of ≈ 0.72 in the $a_* = 0$ simulation and a minimum of ≈ 0.73 in the $a_* = 0.2$ simulation at the respective r_{isco} .

The loss of angular momentum (Fig. 4, 5) increases the inflowing mass accretion rate \dot{M}_{in} (Fig. 6). The total mass accretion rate is calculated as

$$\dot{M} = 2\pi \int_0^\pi \sqrt{-g} \rho u^r d\theta, \quad (14)$$

where u^r is the radial 4-velocity component of the gas, and ρ its density. For the spacetime diagram of the inflowing mass accretion rate shown in Fig. 6, we subtract the outflowing mass rate from the total mass accretion rate to isolate the mass flowing towards the neutron star. When the impact of the burst is still negligible, $\dot{M}_{\text{in}} \approx 10^{16}$ g s^{-1} across both simulated discs. Between $t \sim 0.5 - 1$ s, the inflow-

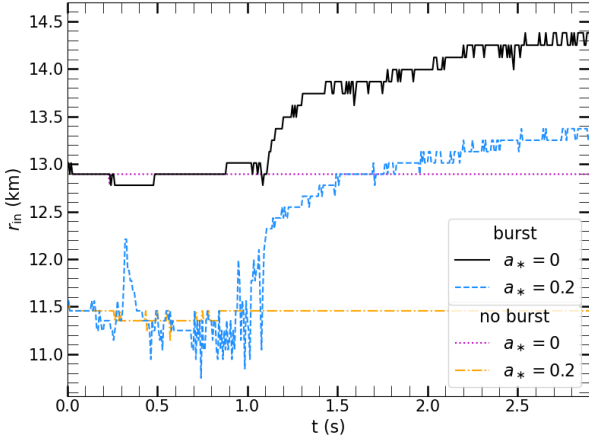


Figure 3. Movement of the inner accretion disc radius. The inner radius is set at a radius where the surface density is closest to $2.5 \times 10^2 \text{ g cm}^{-2}$. While r_{in} remains at $\approx r_{\text{isco}}$ in the $a_* = 0$ (magenta dotted line) and $a_* = 0.2$ (orange dot-dashed line) no-burst simulations, r_{in} recedes outward by $\approx 1.6 \text{ km}$ in the $a_* = 0$ (black solid line) and by $\approx 2.2 \text{ km}$ in the $a_* = 0.2$ (blue dashed line) burst simulations.

ing mass accretion rate temporarily increases in the $a_* = 0.2$ burst simulation (Fig. 6, right panel) due to transient numerical effects. Neglecting these effects, the inflowing mass accretion rate increases with increasing burst luminosity at $t \gtrsim 1 \text{ s}$ in both simulations. Similar to the Ω evolution, the inflowing mass accretion rate does not increase smoothly but fluctuates. Moreover, the \dot{M}_{in} enhancement appears to be concentrated in two regions of the simulation space at a given instance of time, which is especially visible in the $a_* = 0.2$ burst simulation (Fig. 6, right panel). The region of enhanced \dot{M}_{in} closer to the neutron star is between the star and the accretion disc and the second region starts at the disc. The space of enhanced \dot{M}_{in} increasingly extends towards larger radii as the burst strengthens and the \dot{M}_{in} enhancement drains the inner disc region (also visualized by the red regions in Fig. 2, bottom row).

Even though a prograde neutron star spin should weaken the PR drag, the inflowing mass accretion rate at the r_{isco} (black dashed vertical lines in Fig. 6) is actually higher in the $a_* = 0.2$ simulation than in the $a_* = 0$ one (Fig. 7). The strengthening burst increases PR drag and raises \dot{M}_{in} compared to the no-burst simulation by a factor of ≈ 7.9 if $a_* = 0$ (solid black line) and by ≈ 11.2 if $a_* = 0.2$ (blue dashed line) at the respective r_{isco} .

The greater inflowing mass accretion rate enhancement in the $a_* = 0.2$ simulation than in the $a_* = 0$ one at their respective r_{isco} (Fig. 7) is due to different disc structural evolutions. The thin accretion disc equations can be used to approximate \dot{M} as $|\dot{M}| \sim 3\pi\alpha H^2 \Sigma \Omega$ (see also Fragile et al. 2020). The burst radiation heats the discs (Fig. 2) and, since they are pressure supported, inflates them. Besides the increase in height H due to disc inflation, the enhanced \dot{M} due to PR drag lowers the surface density Σ . Due to the different steady state disc structures (see e.g. Fig. 2, upper row), Σ and H evolve differently in the spin and the no-spin burst simulation. For example, the time-averaged surface densities at the respective r_{in} (e.g., Fig. 3) decrease during the burst by $\approx 24.2\%$ if $a_* = 0$ and $\approx 17.9\%$ if $a_* = 0.2$ compared to the no-burst simulations. Similarly, the time-averaged heights increase due to the burst ≈ 4.3 times if $a_* = 0$ and ≈ 4.8 times if $a_* = 0.2$ (after its transient event at $t \sim 1 \text{ s}$).

4 ANGULAR FORCE DUE TO PR DRAG

The results presented in Section 3 seemingly disagree with the expectation that neutron star spin should reduce PR drag. However, when evaluating the effect of PR drag, one must not only consider its spin-, but also its distance-, dependence. The $a_* = 0.2$ disc is closer to the neutron star and therefore experiences a stronger burst flux, which offsets the impact of spin. To illustrate this point, we follow Klacka (1992) and calculate the force due to PR drag as outlined below.

In the derivation of Klacka (1992), the unprimed variables are measured in the frame of the irradiating source (the neutron star) and the primed variables in the frame of the moving particle (the disc material). If the primed frame moves with 3-velocity, \mathbf{v} , variables convert between frames through the usual Lorentz transformations (e.g., Misner et al. 1973)

$$x' = \Lambda x, \quad (15)$$

where Λ is the transformation matrix

$$\begin{pmatrix} \gamma & -\gamma v_x & -\gamma v_y & -\gamma v_z \\ -\gamma v_x & 1 + (\gamma - 1) \frac{v_x^2}{v^2} & (\gamma - 1) \frac{v_x v_y}{v^2} & (\gamma - 1) \frac{v_x v_z}{v^2} \\ -\gamma v_y & (\gamma - 1) \frac{v_x v_y}{v^2} & 1 + (\gamma - 1) \frac{v_y^2}{v^2} & (\gamma - 1) \frac{v_z v_y}{v^2} \\ -\gamma v_z & (\gamma - 1) \frac{v_x v_z}{v^2} & (\gamma - 1) \frac{v_z v_y}{v^2} & 1 + (\gamma - 1) \frac{v_z^2}{v^2} \end{pmatrix} \quad (16)$$

and γ is the Lorentz factor $(1 - v^2)^{-1/2}$. The primed vectors convert to the unprimed ones with the inverse of the transformation matrix, $x = \Lambda^{-1} x'$. As an example, the components of the position vector (t, \mathbf{x}) transform as

$$\begin{aligned} t' &= \gamma (t - \mathbf{v} \cdot \mathbf{x}) \\ \mathbf{x}' &= \mathbf{x} + \left[\frac{\gamma - 1}{v^2} (\mathbf{v} \cdot \mathbf{x}) - \gamma t \right] \mathbf{v} \end{aligned} \quad (17)$$

and back through

$$\begin{aligned} t &= \gamma (t' + \mathbf{v} \cdot \mathbf{x}') \\ \mathbf{x} &= \mathbf{x}' + \left[\frac{\gamma - 1}{v^2} (\mathbf{v} \cdot \mathbf{x}') + \gamma t' \right] \mathbf{v}. \end{aligned} \quad (18)$$

We assume that the disc particles move on Keplerian orbits with a 3-velocity (e.g., Abramowicz & Fragile 2013)

$$\mathbf{v} = \frac{\sqrt{M}}{r^{3/2} + aM^{1/2}} \hat{e}_\phi, \quad (19)$$

where \hat{e}_ϕ is a unit vector in the ϕ direction.

In the frame of a disc particle, the incident irradiation energy is

$$E'_i = n' A' \epsilon', \quad (20)$$

with n' being the number density of photons, A' the particle cross section and ϵ' the energy per photon. We assume that the particle's cross section is the Thomson cross section, σ_T . The incident 3-momentum corresponding to radiation energy E'_i is

$$\mathbf{p}'_i = n' A' \epsilon' \hat{\mathbf{S}}', \quad (21)$$

where the unit Poynting vector, $\hat{\mathbf{S}}$, points in the direction of the irradiation and consists of the normalized stress energy tensor components R^{0i} (eq. 10). For this calculation, we only consider motion in the equatorial plane and set $\theta = \pi/2$. We can relate $\hat{\mathbf{S}}$ to $\hat{\mathbf{S}}'$ by considering the transformation of (E_i, \mathbf{p}_i) to the disc particle frame

$$\begin{aligned} E'_i &= E_i \gamma (1 - \mathbf{v} \cdot \hat{\mathbf{S}}) \\ \mathbf{p}'_i &= E_i \left\{ \hat{\mathbf{S}} + \left[\frac{\gamma - 1}{v^2} (\mathbf{v} \cdot \hat{\mathbf{S}}) - \gamma \right] \mathbf{v} \right\}. \end{aligned} \quad (22)$$

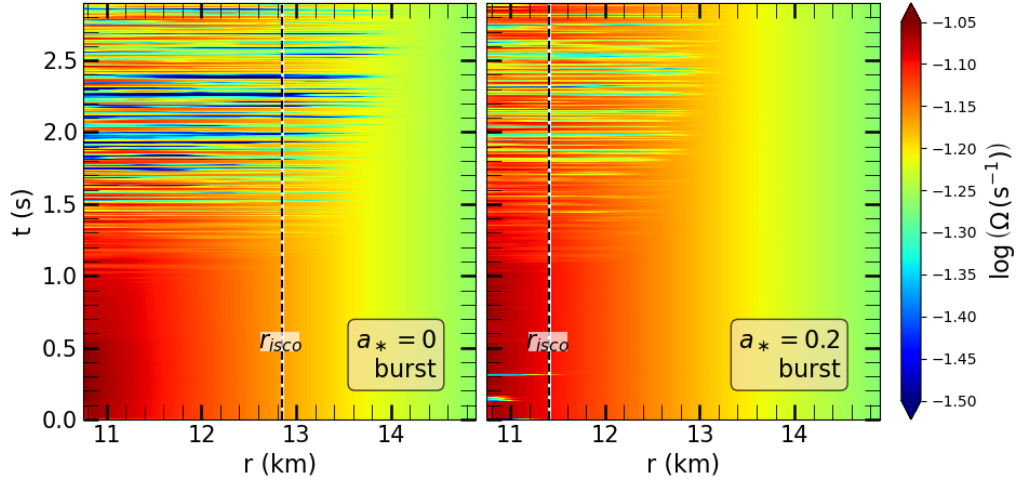


Figure 4. The logarithm of the density-weighted angular frequencies during the burst. As the burst strength increases, the increasing PR drag decreases the angular frequencies in both the $a_* = 0$ (left panel) and the $a_* = 0.2$ (right panel) burst simulations. Due to the numerical nature of the simulations, the decrease is not smooth but fluctuates. The region of decreased Ω extends towards larger radii over time as the strengthening burst drains the inner disc region. The dashed vertical lines show the respective r_{isco} , where Ω is measured in Fig. 5.

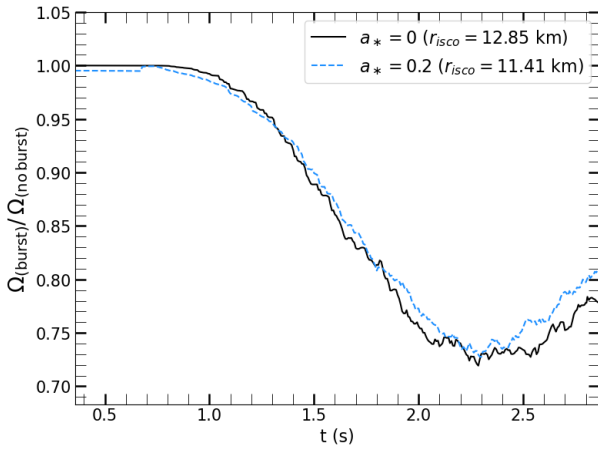


Figure 5. Ratio of the density-weighted angular velocities. The moving averages of the velocities, measured at the respective r_{isco} (dashed black lines in Fig. 4) depending on the simulation, were calculated with an average window of $\Delta t \approx 0.71$ s. The angular frequencies decrease by a similar factor in the $a_* = 0$ (black solid line) and the $a_* = 0.2$ (blue dashed line) simulations, and reach their minima at about the time the burst peaks.

With equations (20), (21) and (22), $\hat{\mathbf{S}}'$ can be expressed as

$$\hat{\mathbf{S}}' = \frac{1}{w} \left\{ \hat{\mathbf{S}} + \left[\frac{\gamma - 1}{\mathbf{v}^2} (\mathbf{v} \cdot \hat{\mathbf{S}}) - \gamma \right] \mathbf{v} \right\}, \quad (23)$$

where

$$w = \gamma (1 - \mathbf{v} \cdot \hat{\mathbf{S}}). \quad (24)$$

The energy per photon, ϵ , transforms analogous to the incident radiation energy (eq. 22), $\epsilon' = \epsilon w$. The photon number density, n , is part of the 4-current vector $(n, n\hat{\mathbf{S}})$, so it also transforms as $n' = nw$. The initial energy can thus be rewritten as

$$E_i = \frac{E'_i}{w} = \frac{n' A' \epsilon'}{w} = wn\epsilon\sigma'_T. \quad (25)$$

We assume that the disc particle completely absorbs the radiation and reemits it isotropically in its own frame. The outgoing momentum \mathbf{p}'_o is thus zero and the outgoing energy $E'_o = E'_i$ in the particle frame. The outgoing 4-vector $(E'_o, \mathbf{0})$ in the neutron star frame is (using eq. 22)

$$E_o = E'_i \gamma = \left[E_i \gamma (1 - \mathbf{v} \cdot \hat{\mathbf{S}}) \right] \gamma \quad (26)$$

$$\mathbf{p}_o = E'_i \gamma \mathbf{v} = \left[E_i \gamma (1 - \mathbf{v} \cdot \hat{\mathbf{S}}) \right] \gamma \mathbf{v}.$$

The change in momentum of the radiation per unit time is $\mathbf{p}_o - \mathbf{p}_i$. The momentum exchange exists only between the radiation and the disc particle. For the disc particle, the change in momentum \mathbf{p}_p is (using eq. 25 and 26)

$$\begin{aligned} \frac{d\mathbf{p}_p}{d\tau} &= \mathbf{p}_i - \mathbf{p}_o = E_i \hat{\mathbf{S}} - E_i \gamma^2 \mathbf{v} (1 - \mathbf{v} \cdot \hat{\mathbf{S}}) \\ &= E_i (\hat{\mathbf{S}} - \gamma \mathbf{v} w) = wn\epsilon\sigma'_T (\hat{\mathbf{S}} - \gamma \mathbf{v} w). \end{aligned} \quad (27)$$

Since $d/d\tau = \gamma d/dt$, the 3-force, \mathbf{F}_p , exerted on the disc particle is

$$\mathbf{F}_p = \frac{d\mathbf{p}_p}{dt} = \gamma^{-1} wn\epsilon\sigma'_T (\hat{\mathbf{S}} - \gamma \mathbf{v} w). \quad (28)$$

For the $n\epsilon$ term in eq. (28), we use the intensity parameter (Bakala et al. 2019)

$$\Phi^2 = \frac{L}{4\pi\sqrt{R_{b,q}(r)}}. \quad (29)$$

Fig. 8 shows the magnitude of the angular component of \mathbf{F}_p (eq. 28), F^ϕ , at the peak luminosity 10^{38} ergs s^{-1} . Comparing the angular force at the same radius gives the expected result that F^ϕ is stronger if $a_* = 0$ (solid black line) than if $a_* = 0.2$ (blue dashed line). However, the $a_* = 0.2$ disc is closer to the neutron star (left red dotted line) than the $a_* = 0$ disc (right red dotted line), offsetting the impact of spin. The angular force is stronger by a factor of ≈ 1.43 for the $a_* = 0.2$ disc than for the $a_* = 0$ one at their respective r_{isco} . This factor approximately matches the difference in inflowing mass accretion rate enhancement of the spin versus the no-spin simulation.

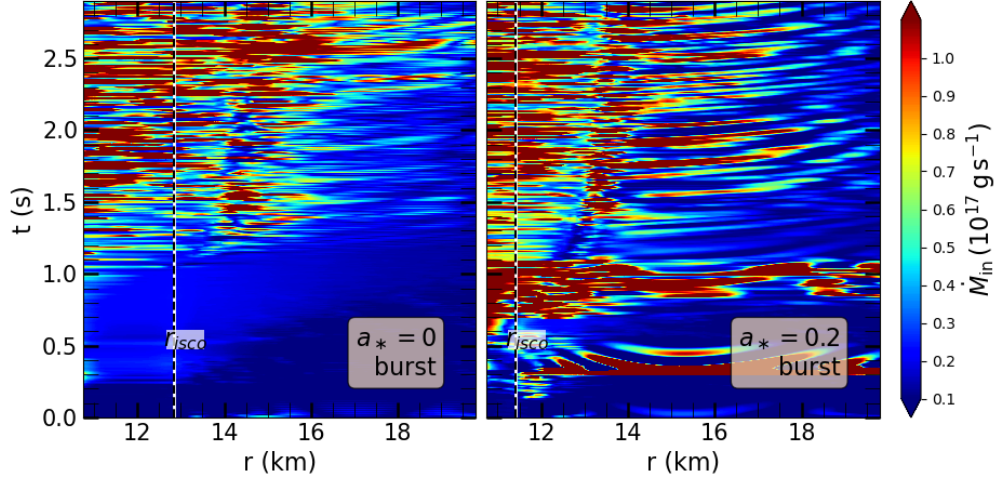


Figure 6. Same as Fig. 4, but showing the mass accretion rate of inflowing material. Initially, $\dot{M}_{in} \approx 10^{16} \text{ g s}^{-1}$ across both simulated discs. After ≈ 1 s, \dot{M}_{in} is significantly enhanced in both the $a_* = 0$ (left panel) and the $a_* = 0.2$ (right panel) burst simulations. The spike in \dot{M}_{in} at $t \sim 0.5 - 1$ s in the $a_* = 0.2$ simulation is a transient numerical effect. The enhanced \dot{M}_{in} after $t \sim 1$ s extends towards larger radii over time as the burst strengthens and the \dot{M}_{in} enhancement drains the inner disc region.

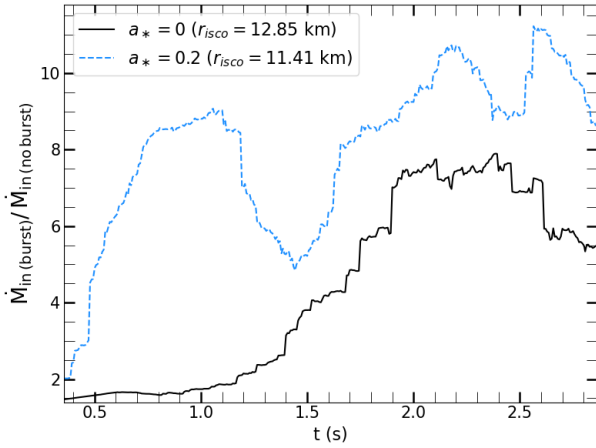


Figure 7. Same as Fig. 5, but showing the inflowing mass accretion rate ratios between burst and no-burst simulations. The inflowing mass accretion rate increases during the burst for both the no-spin (solid, black line) and the spin (blue, dashed line) simulations at their respective r_{isco} (dashed vertical lines in Fig. 6). The increase in \dot{M}_{in} for $a_* = 0.2$ at $t \sim 1$ s is due to transient numerical effects.

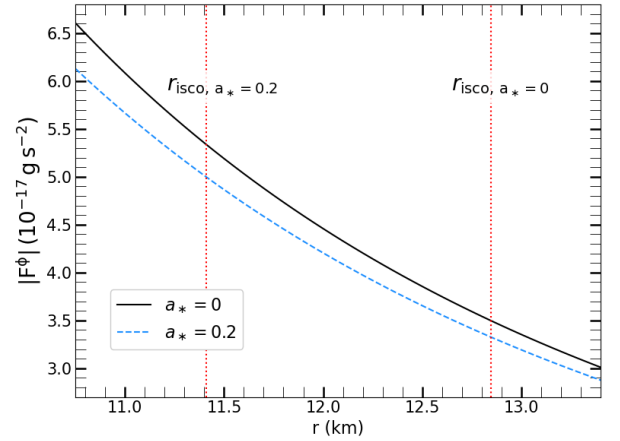


Figure 8. Angular force in the equatorial plane due to PR drag at the peak of the burst (eq. 28). The $a_* = 0$ disc (black solid line) loses more angular momentum at a specific radius than the $a_* = 0.2$ disc (blue dashed line). However, because the $a_* = 0.2$ disc starts closer to the neutron star (left red dotted line) than the $a_* = 0$ disc (right red dotted line), it experiences a higher flux, which offsets the impact of spin.

Thus, the distance dependence of the PR drag can explain why the mass accretion rate in the spin simulation is more enhanced than in the no-spin simulation. The closer distance of the disc to the neutron star in the $a_* = 0.2$ simulation outweighs the reduction of PR drag by spin, so that the disc in the spin simulation experiences a stronger PR drag than in the no-spin simulation.

5 DISCUSSION

In the burst simulations presented in Section 3, increased PR drag removes angular momentum from the accretion disc (Fig. 4, 5), which increases the mass accretion rate during the burst (Fig. 6, 7). An enhanced mass accretion rate is a potential explanation for an increase

in persistent emission during observed X-ray bursts, which can be quantified via a normalization factor, f_a (e.g., Worpel et al. 2013, 2015). The normalization factors obtained from fitting observational data depend on the burst strength. They tend to peak at $\lesssim 4$ for non-photospheric radius expansion bursts (e.g., Worpel et al. 2015; Keek et al. 2018; Güver et al. 2022a,b), but can reach values ≥ 10 for photospheric radius expansion bursts (e.g., Chen et al. 2019; Jaisawal et al. 2019; Roy et al. 2021). However, how the normalization factor translates into changes in \dot{M} remains unclear. Hence, the inflowing mass accretion rate enhancements of ≥ 8 at the respective r_{isco} of the burst simulations (Fig. 7) are quite plausible.

The normalization factor has also been used to account for a soft excess in the X-ray spectra of bursts (e.g., Keek et al. 2018; Bult et al. 2019; Güver et al. 2022a,b). As Fig. 6 and 7 show, the inflowing mass

accretion rate is significantly enhanced in spin and no-spin environments and could therefore contribute to the soft excess. However, another contribution to the soft excess may come from the reflection signature of the accretion disc (e.g., [Speicher et al. 2022](#)), which is disc temperature dependent. While moderate disc heating increases the soft excess, too much heating can move the soft X-ray emission to higher energies and thus lower the soft excess. Given warmer steady-state temperatures (right panel, upper row in Fig. 2), the $a_* = 0.2$ disc is hotter than the $a_* = 0$ disc during the burst (Fig. 2). A highly spinning star with a correspondingly hot disc may therefore emit low amounts of soft excess through reflection. Combined with an increased PR drag due to an accretion disc closer to the neutron star, the relative importance of PR drag in explaining the soft excess compared to reflection could increase with increasing neutron star spin.

6 CONCLUSIONS

X-ray burst observations often feature an increase in persistent emission, which is usually quantified by a normalization factor, f_a (e.g., [Worpel et al. 2013, 2015](#); [Jaisawal et al. 2019](#); [Güver et al. 2022b](#)). Moreover, f_a has been used to explain a soft excess in the spectra of bursts (e.g., [Keek et al. 2018](#); [Bult et al. 2019](#); [Güver et al. 2022a,b](#)). The normalization factor is often linked to an increased mass accretion rate due to increased PR drag. While studies by [Walker & Meszaros \(1989\)](#) and [Fragile et al. \(2020\)](#) showed that PR drag can significantly enhance \dot{M} , [Walker \(1992\)](#) alluded to a reduced impact of PR drag in the presence of neutron star spin.

In this paper, we studied the role of spin on PR drag during X-ray bursts by simulating thin accretion discs in non-spinning and spinning neutron star environments. We showed that while spin reduces the PR drag at a given radius, since the disc around a spinning star reaches closer to the surface, it actually experiences a stronger radiative flux, which offsets the PR drage reduction due to spin (Section 4). Thus in both the no-spin and the spin simulations, PR drag is strong enough to remove angular momentum from the disc, which enhances the mass accretion rate and drains the inner disc region (section 3). PR drag therefore remains a viable explanation for the increased persistent emission and soft excess during X-ray bursts. In addition, the X-ray burst heats the disc in the spin simulation to higher final temperatures than in the no-spin one due to different steady-state structures, which could lower the importance of reflection in contributing to the soft excess for highly spinning neutron star systems (Section 5).

ACKNOWLEDGEMENTS

P.C. Fragile acknowledges support from National Science Foundation grants AST-1907850 and PHY-1748958. J. Speicher acknowledges support from the NDSEG fellowship.

DATA AVAILABILITY

The data underlying this article will be shared on reasonable request to the corresponding author.

REFERENCES

Abramowicz M. A., Fragile P. C., 2013, *Living Reviews in Relativity*, 16, 1

- Anninos P., Fragile P. C., Salmonson J. D., 2005, *ApJ*, 635, 723
- Bakala P., De Falco V., Battista E., Goluchová K., Lančová D., Falanga M., Stella L., 2019, *Phys. Rev. D*, 100, 104053
- Ballantyne D. R., Strohmayer T. E., 2004, *ApJ*, 602, L105
- Barrière N. M., et al., 2015, *ApJ*, 799, 123
- Bassa C. G., et al., 2017, *ApJ*, 846, L20
- Bult P., et al., 2019, *ApJ*, 885, L1
- Bult P., et al., 2022, *ApJ*, 940, 81
- Chakrabarty D., Morgan E. H., Muno M. P., Galloway D. K., Wijnands R., van der Klis M., Markwardt C. B., 2003, *Nature*, 424, 42
- Chen Y. P., et al., 2019, *Journal of High Energy Astrophysics*, 24, 23
- Cook G. B., Shapiro S. L., Teukolsky S. A., 1994, *ApJ*, 424, 823
- Degenaar N., Miller J. M., Wijnands R., Altamirano D., Fabian A. C., 2013, *ApJ*, 767, L37
- Degenaar N., et al., 2018, *Space Sci. Rev.*, 214, 15
- Fragile P. C., Gillespie A., Monahan T., Rodriguez M., Anninos P., 2012, *ApJS*, 201, 9
- Fragile P. C., Olejar A., Anninos P., 2014, *ApJ*, 796, 22
- Fragile P. C., Etheridge S. M., Anninos P., Mishra B., Kluźniak W., 2018, *ApJ*, 857, 1
- Fragile P. C., Ballantyne D. R., Blankenship A., 2020, *Nature Astronomy*, 4, 541
- Fujimoto M. Y., Hanawa T., Miyaji S., 1981, *ApJ*, 247, 267
- Galeev A. A., Rosner R., Vaiana G. S., 1979, *ApJ*, 229, 318
- Galloway D. K., Keek L., 2021, in Belloni T. M., Méndez M., Zhang C., eds, *Astrophysics and Space Science Library* Vol. 461, *Timing Neutron Stars: Pulsations, Oscillations and Explosions*. pp 209–262 ([arXiv:1712.06227](#)), doi:10.1007/978-3-662-62110-3_5
- Galloway D. K., Muno M. P., Hartman J. M., Psaltis D., Chakrabarty D., 2008, *ApJS*, 179, 360
- Güver T., et al., 2022a, *MNRAS*, 510, 1577
- Güver T., et al., 2022b, *ApJ*, 935, 154
- Hessels J. W. T., Ransom S. M., Stairs I. H., Freire P. C. C., Kaspi V. M., Camilo F., 2006, *Science*, 311, 1901
- Hirose S., Krolik J. H., Blaes O., 2009, *ApJ*, 691, 16
- Inogamov N. A., Sunyaev R. A., 1999, *Astronomy Letters*, 25, 269
- Inogamov N. A., Sunyaev R. A., 2010, *Astronomy Letters*, 36, 848
- Jaisawal G. K., et al., 2019, *ApJ*, 883, 61
- Ji L., Zhang S., Chen Y., Zhang S.-N., Torres D. F., Kretschmar P., Li J., 2014, *ApJ*, 782, 40
- Keek L., Ballantyne D. R., Kuulkers E., Strohmayer T. E., 2014a, *ApJ*, 789, 121
- Keek L., Ballantyne D. R., Kuulkers E., Strohmayer T. E., 2014b, *ApJ*, 797, L23
- Keek L., Iwakiri W., Serino M., Ballantyne D. R., in't Zand J. J. M., Strohmayer T. E., 2017, *ApJ*, 836, 111
- Keek L., et al., 2018, *ApJ*, 855, L4
- Klacka J., 1992, *Earth Moon and Planets*, 59, 41
- Koliogiannis P. S., Moustakidis C. C., 2020, *Phys. Rev. C*, 101, 015805
- Kubota A., Makishima K., 2004, *ApJ*, 601, 428
- Kubota A., Ebisawa K., Makishima K., Nakazawa K., 2005, *ApJ*, 631, 1062
- Kuulkers E., den Hartog P. R., in't Zand J. J. M., Verbunt F. W. M., Harris W. E., Cocchi M., 2003, *A&A*, 399, 663
- Lewin W. H. G., van Paradijs J., Taam R. E., 1993, *Space Sci. Rev.*, 62, 223
- Maccarone T. J., Coppi P. S., 2003, *A&A*, 399, 1151
- Misner C. W., Thorne K. S., Wheeler J. A., 1973, *Gravitation*. W.H. Freeman and Company
- Narayan R., Heyl J. S., 2003, *ApJ*, 599, 419
- Norris J. P., Bonnell J. T., Kazanas D., Scargle J. D., Hakkila J., Giblin T. W., 2005, *ApJ*, 627, 324
- Novikov I. D., Thorne K. S., 1973, in *Black Holes (Les Astres Occlus)*. pp 343–450
- Patruno A., Haskell B., Andersson N., 2017, *ApJ*, 850, 106
- Popham R., Sunyaev R., 2001, *ApJ*, 547, 355
- Robertson H. P., 1937, *MNRAS*, 97, 423
- Roy P., Beri A., Bhattacharyya S., 2021, *MNRAS*, 508, 2123
- Sánchez-Fernández C., Kajava J. J. E., Poutanen J., Kuulkers E., Suleimanov V. F., 2020, *A&A*, 634, A58

- Schwarzschild M., Härm R., 1965, [ApJ](#), **142**, 855
- Shafee R., McKinney J. C., Narayan R., Tchekhovskoy A., Gammie C. F., McClintock J. E., 2008, [ApJ](#), **687**, L25
- Shakura N. I., Sunyaev R. A., 1973, [A&A](#), **24**, 337
- Sibgatullin N. R., Sunyaev R. A., 1998, [Astronomy Letters](#), **24**, 774
- Sądowski A., Narayan R., Tchekhovskoy A., Zhu Y., 2013, [MNRAS](#), **429**, 3533
- Speicher J., Ballantyne D. R., Malzac J., 2020, [MNRAS](#), **499**, 4479
- Speicher J., Ballantyne D. R., Fragile P. C., 2022, [MNRAS](#), **509**, 1736
- Strohmayer T. E., Brown E. F., 2002, [ApJ](#), **566**, 1045
- Walker M. A., 1992, [ApJ](#), **385**, 642
- Walker M. A., Meszaros P., 1989, [ApJ](#), **346**, 844
- Worpel H., Galloway D. K., Price D. J., 2013, [ApJ](#), **772**, 94
- Worpel H., Galloway D. K., Price D. J., 2015, [ApJ](#), **801**, 60
- Yoon S. C., Langer N., van der Sluys M., 2004, [A&A](#), **425**, 207
- Zdziarski A. A., Gierliński M., 2004, [Progress of Theoretical Physics Supplement](#), **155**, 99

This paper has been typeset from a $\text{\TeX}/\text{\LaTeX}$ file prepared by the author.